Journal of
Materials Chemistry A

ROYAL SOCIETY
OF CHEMISTRY

PAPER

View Article Online
View Journal | View Issue

Check for updates

Cite this: *J. Mater. Chem. A*, 2025, **13**, 35847

A carbon-based hybrid catalytic-protective overlayer for kesterite photocathodes for solar water splitting

Mingrui He, †[a] Umesh P. Suryawanshi,†[b] Seung Wook Shin,†[c] Yiming Xia,[a] Priyank V. Kumar, [d] Jialiang Huang,[a] Jialin Cong,[a] Hongjae Shim,[a] Youseong Park,[b] Jun Sung Jang, [b] Jin Hyeok Kim, *[b] Mahesh P. Suryawanshi *[a] and Xiaojing Hao*[a]

Received 8th January 2025
Accepted 26th August 2025

DOI: 10.1039/d5ta00165j

rsc.li/materials-a

Developing stable and efficient photocathodes with low-cost components is crucial for advancing the commercialization of photoelectrochemical (PEC) water splitting devices, specifically for the hydrogen evolution reaction (HER). In this work, we present a cost-effective solution-processed hybrid layer composed of fullerene (C_{60}) grafted onto nitrogen and sulfur-doped graphene (NSG), which serves as a catalytic-protective overlayer for the earth-abundant kesterite $Cu_2ZnSn(S,Se)_4$ (CZTSSe) photocathode in an acidic environment. The resulting CZTSSe/CdS/C_{60}-NSG/Pt photocathode exhibits a current density of −27.7 mA cm^{-2} at 0 V *vs.* the reversible hydrogen electrode (RHE), a half-cell solar-to-hydrogen efficiency exceeding 3%, and an onset potential of 0.51 V, while retaining 80% of its initial current density after 10 h of operation. Spectroscopic analyses and density functional theory studies indicate that the C_{60}-NSG hybrid layer improves carrier lifetime, facilitates efficient charge transfer, and provides catalytic sites with Gibbs free energy close to thermoneutral for adsorbed H species, leading to higher HER activity and operational stability. Our findings highlight the potential of employing a cost-effective solution-processed 'carbon-based' hybrid catalytic-protective layer on photocathodes for solar water splitting.

1. Introduction

Hydrogen (H_2) is an environmentally friendly energy carrier that has the potential to reduce our reliance on fossil fuels. Traditional methods of H_2 production, such as coal and oil gasification or steam methane reforming, generate massive amounts of carbon dioxide, exacerbating climate change.[1,2] Photoelectrochemical (PEC) cells, which harness sunlight to split water into H_2 and O_2, offer a promising and sustainable approach to H_2 production.[3,4] The key to efficient PEC cells is high-performance photoelectrodes that can absorb a broad spectrum of sunlight, facilitate rapid charge transfer at the semiconductor/electrolyte interface, and maintain long-term stability.

Various materials have been explored as photocathodes for PEC cells, including metal oxides,[5,6] halide perovskites,[7–9] III–IV compounds,[10] Si,[11,12] and chalcogenides such as chalcopyrite $Cu(In,Ga)Se_2$ (CIGS),[13,14] $Sb_2(S,Se)_3$ (ref. 15 and 16), and kesterite $Cu_2ZnSn(S,Se)_4$ (CZTSSe).[17,18] Among these, metal oxides have limited light absorption due to their wide band gap energy (E_g) (>2 eV), and halide perovskites suffer from instability in aqueous environments. Although III–V or Si-based semiconductors have achieved excellent photocurrent densities and high solar-to-hydrogen (STH) efficiencies, their high cost and device complexity are significant hindrances for mass commercialization.[19,20]

CZTSSe, an earth-abundant, low-cost, and less toxic material, stands out due to its tunable E_g (1.0–1.5 eV) and ability to absorb a maximum portion of the broad range of the solar spectrum.[21] Notably, its promise in photovoltaic technology has already been proved.[22–24] However, CZTSSe-based photocathodes lack stability under aqueous conditions, requiring a corrosion-resistant protective layer that does not impede the effective transfer of photogenerated carriers. Dense TiO_2 deposited *via* atomic layer deposition (ALD) has been used as such a protective layer, often combined with noble metal-based catalysts like Pt to improve the performance and stability of chalcogenide photocathodes.[25–27] However, TiO_2 has poor adhesion to the top

---

[a] *School of Photovoltaic and Renewable Energy Engineering, University of New South Wales, New South Wales, Sydney, NSW 2052, Australia. E-mail: m.suryawanshi@unsw.edu.au; xj.hao@unsw.edu.au*

[b] *Department of Materials Science and Engineering, Chonnam National University, Gwangju 61186, Republic of Korea. E-mail: jinhyeok@chonnam.ac.kr*

[c] *Rural Research Institute Korea Rural Community Corporation, Ansan-si 15634, South Korea*

[d] *School of Chemical Engineering, University of New South Wales, New South Wales, Sydney NSW 2052, Australia*

† These authors contributed equally to this work.

catalyst (*e.g.*, Pt), leading to catalyst aggregation and desorption in the electrolyte. Furthermore, the high photoreduction level of TiO_2, low hydrogen evolution reaction (HER) rate, and poor charge transfer in thick TiO_2 layers on the photoelectrode demand additional modification of the photoelectrode surface to facilitate efficient photoelectron transfer.[28] Though ALD HfO_2 has shown promise in protecting the Cu_2ZnSnS_4 (CZTS) photocathode, the slow deposition rate of ALD limits its productively.[29] Thus, there is a need for facile and cost-effective deposition methods and materials to modify and protect chalcogenide-based photocathodes.

Carbon allotropes fullerene (C_{60}), carbon nanotubes, and graphene are promising alternatives for protecting photocathodes due to their low-cost, earth abundance, high electrical conductivity, and excellent stability in aqueous solutions.[28,30–37] C_{60}, in particular, is known for its ability to promote photogenerated charge separation and protect semiconductor-based photoelectrodes from photocorrosion.[38–40] Studies have demonstrated that incorporating C_{60} into TiO_2 nanostructures enhances photocatalytic activity by facilitating charge separation and providing actives sites for the HER.[27,41] Similarly, graphene-based materials like reduced graphene oxide (rGO) have been shown to improve the stability and PEC performance of chalcogenide photocathodes by providing adhesion sites for catalysts.[42] Despite the advantages of carbon-based materials, their work function energies are generally lower than those of chalcogenides, creating a large conduction band offset (CBO) that hinders photoinjected electron transfer and limits PEC performance.[43–45] A promising strategy to overcome the limitations of individual carbon allotropes is the development of carbon-based hybrid materials, which can combine distinct dimensionalities and surface chemistries while enabling tunable work function energies for improved interfacial charge transfer. Additionally, heteroatom doping in carbon-based materials has been shown to enhance catalytic activity by introducing more active sites and improving operational stability.[46–48] Despite these advantages, systematic investigations into C_{60} and graphene-based hybrid protective layers or co-catalysts, particularly for use with chalcogenide photocathodes such as CZTSSe, remain limited.

In this work, we demonstrate that a hybrid material composed of C_{60} and nitrogen (N) and sulfur (S) co-doped graphene (NSG), denoted as C_{60}-NSG hybrid, functions as an effective catalytic-protective layer when integrated onto a CZTSSe photocathode (CZTSSe/CdS/C_{60}-NSG/Pt). This hybrid layer significantly enhances the PEC performance and improves operational stability. The C_{60}-NSG hybrid facilitates efficient collection and transfer of photogenerated electrons while suppressing charge recombination, thereby reducing voltage loss. To elucidate the underlying mechanisms, density functional theory (DFT) calculations combined with experimental characterization were carried out to investigate the work functions and catalytic properties of the C_{60}-NSG hybrid. Additionally, DFT-derived free energy diagrams of key reaction intermediates reveal the catalytic role of the C_{60}-NSG hybrid in promoting efficient electron transfer during the HER.

2. Experimental details

2.1. Synthesis of the CZTSSe photocathode

CZTSSe photocathodes were prepared by a two-step (precursor deposition followed by sulfo-selenization) fabrication process. Metallic precursor thin films were deposited by sequential sputtering of Zn, Sn and Cu metallic targets on molybdenum (Mo)-coated soda-lime glass. Subsequently, the metallic precursor thin films were annealed in a conventional tube furnace under an Ar atmosphere at 300 °C for 60 minutes, aiming to form pre-alloyed precursors (Cu–Zn and Cu–Sn alloys). After that, 0.002 g sulfur and 0.198 g selenium powders and the pre-alloyed precursor thin films were placed in a graphite box in a closed isothermal chamber system and annealed at 520 °C for 10 min. Before the deposition of the CdS buffer layer, each CZTSSe thin film was etched with 0.2 M potassium cyanide at room temperature for 120 s, and rinsed using deionized water (DI) water for 60 s. After that, the CdS buffer layer with 25 nm thickness was deposited onto the CZTSSe absorber layers *via* the chemical bath deposition method using a precursor solution consisting of 0.0031 M $CdSO_4$, 1.9 M ammonia, and 0.25 M thiourea at 60 °C for 14.5 min.

2.2. Synthesis of GO and NSG

First, GO was synthesized using a modified Hummer's method.[49] In particular, natural graphite flakes (3.0 g) were added to conc. H_2SO_4 (70 mL) under stirring. Then, $KMnO_4$ was added slowly and stirred for 0.5 h at 40 °C. Then distilled water (150 mL) was added to the system and stirred for 15 min at 95 °C. The system was further treated with 30% H_2O_2 (15 mL), followed by filtering and washing with HCl and distilled water (1 : 10), and dried overnight at 60 °C. The synthesis of NSG was carried out following our previous recipe with slight modifications.[50] In a typical synthesis, ∼200 mg of GO was dispersed in 50 mL DI water, and 630 mg of thiourea was added into the solution and stirred for 4 h. The reaction was then transferred into a Teflon-lined autoclave and heated at 160 °C for 12 h. The resulting black powder was collected and alternately washed with DI water and ethanol followed by overnight drying at room temperature in a vacuum oven. The samples were further annealed at 700 °C in an Ar atmosphere for 1 h before being used for further characterization.

2.3. Synthesis of the C_{60}-NSG hybrid

The synthesis of the C_{60}-NSG hybrid was carried out following a previous recipe with slight modifications.[51] In a typical process, NSG nanosheets (5 mg) were dispersed in toluene (10 mL) under an Ar atmosphere in a round bottom flask. In the next step, 2.5 M of 0.8 mL *n*-butyllithium (*n*-BuLi) in hexane was added dropwise into the above solution and sonicated for 2 h. Further, C_{60} (45 mg) in toluene was added to the above reaction mixture and sonicated for 3 h followed by overnight stirring. The following day, a few drops of methanol were added to terminate the reaction. The resultant black solid (C_{60}-grafted NSG, hereafter referred to as the 'C_{60}-NSG hybrid') was rinsed twice using methanol and then dried in a vacuum at 60 °C overnight for further characterization.

2.4. Deposition of the C_{60}-NSG hybrid onto the CZTSSe/CdS absorber

The as-prepared C_{60}-NSG hybrid (10 mg) was dispersed in either 1 mL of toluene solution and stirred well to get a homogeneous mixture. Thereafter, the above solution was spin coated on the CZTSSe photocathode with 3000 rpm for 30 s and then dried at 70 °C on a hot plate for 2 min. Different numbers of spin coating cycles (from 1 to 6 cycles) were carried out to deposit the C_{60}-NSG hybrid with different thicknesses. A 10 nm-thick Pt layer on the photoelectrode was prepared using the sputtering technique at room temperature.

2.5. Characterization

The morphologies of the CZTSSe photocathodes were observed using a field emission scanning electron microscope (FE-SEM, FEI Nova Nano SEM 450). Cross-sectional transmission electron microscopy (TEM) specimens were prepared using an FEI x T nova NanoLab 200 FIB system. The microstructure and elemental distribution were investigated using a JEOL F200 with a cold field emission gun scanning TEM. Fourier transform infrared spectroscopy (FTIR) was performed in the range of 4000–500 cm^{-1} at a resolution of 4 cm^{-1} using a PerkinElmer Spectrum 10.5.2 FTIR/NIR system. Photoluminescence (PL) was detected using a Glacier X TE Cooled CCD Spectrometer. The excitation source for time-resolved photoluminescence (TRPL) and PL was a laser operating at a wavelength of 532 nm. TRPL was detected using an id110 VIS 100 MHz Photon Detector operating in free-running mode. Ultraviolet photoelectron spectroscopy (UPS) measurements were conducted with an Axis-Supra using a He I discharge lamp that has 21.2 eV of photon energy under 9 V bias. Raman spectroscopy measurements were carried out using a 532 nm diode laser. X-ray photoelectron spectroscopy (XPS) measurements were conducted utilizing an ESCALAB250Xi (Thermo Scientific) under ultra-high vacuum. An Al Kα monochromatic X-ray source ($h\nu = 1486.68$ eV) with a binding energy scale calibrated using a carbon reference was used. The PEC performances of the fabricated photocathodes were measured using a PARSTAT 4000 (AMETEK Princeton Applied Research) potentiostat. The PEC cell consisted of Ag/AgCl (saturated KCl) as the reference electrode (RE), Pt wire as the counter electrode (CE), and the sample thin films as the working electrode; 0.5 M H_2SO_4 solution (pH ≈ 0.3) was used as the electrolyte. A xenon lamp (AM 1.5G, 100 mW cm^{-2}), a custom-made automatic chopper and a monochromator were used for the illumination. Linear sweep voltammetry (LSV) was conducted at a 2 mV s^{-1} scan rate and the measured potentials were converted to corresponding values *vs.* RHE (reversible hydrogen electrode) using the Nernst equation (eqn (1)):

$$E_{\text{RHE}} = E_{\text{Ag/AgCl}} + 0.059 \times \text{pH} + 0.1976 \tag{1}$$

where, $E_{\text{Ag/AgCl}}$ is the applied potential *vs.* Ag/AgCl, and 0.1976 V is the standard potential of the Ag/AgCl reference electrode at 25 °C.

The half-cell solar-to-hydrogen efficiency (HC-STH) of the photocathode was derived using the following equation (eqn (2)):

$$\text{HC-STH (\%)} = [\text{photocurrent density (mA cm}^{-2}) \times \text{applied bias (V } vs. \text{ RHE)}]/100 \text{ mW cm}^{-2} \times 100\% \tag{2}$$

2.6. Density functional theory (DFT) methods

We used the VASP code for our DFT calculations.[52,53] The core electrons were treated using the projector augmented wave method (PAW),[54] and the Perdew–Burke–Ernzerhof (PBE) exchange–correlation functional was employed. The kinetic energy cut-off for the wavefunctions was 500 eV.[55] All relaxations proceeded until the residual forces on atoms were less than 0.03 eV $Å^{-1}$. A vacuum region greater than 10 Å was used in necessary directions to avoid interaction between the images.

A rectangular unit cell measuring 19.69 Å × 17.05 Å was employed to model NSG, and the corresponding hydrogen evolution reaction at various active sites. The free energy changes upon adsorption were computed using the computational hydrogen electrode (CHE) approach,[56,57] where the free energy of ($H^+ + e^-$) equals $\frac{1}{2}H_2(g)$ for a standard hydrogen electrode (SHE). The free energy of various intermediates is calculated as:

$$G = E_{\text{elec}} + E_{\text{ZPE}} - TS \tag{3}$$

where, E_{elec} is the total electronic energy computed by DFT; E_{ZPE} is the zero-point energy (ZPE), T is the temperature and S is entropy. For H adsorption, the change in free energy is computed as $\Delta G = \Delta E_{\text{elec}} + 0.24$ eV.

3. Results and discussion

3.1. Synthesis and characterization of C_{60}-NSG hybrids

The catalytic-protective C_{60}-NSG hybrid was prepared using a lithiation reaction with *n*-BuLi.[51] It is well known that C_{60} can rapidly undergo nucleophilic addition due to its strong electron affinity.[58] Lithiation of NSG using *n*-BuLi facilitates direct grafting of C_{60} onto the graphitic layer of NSG, enabling the formation of a pure, all carbon C_{60}-NSG hybrid (Fig. 1a). The formation of the C_{60}-NSG hybrid was confirmed by TEM, FTIR, Raman spectroscopy, and XPS characterization studies as shown in Fig. S1 and S2. A high resolution transmission electron microscopy (HR-TEM) image (Fig. S1a) for the C_{60}-NSG hybrid clearly shows a nanosheet surface grafted by nanoparticles of average size ∼20 nm, which are characteristics of C_{60} aggregates, implying strong interconnection between C_{60} and NSG. The scanning TEM (STEM) and elemental mapping images of C_{60}-NSG nanoparticles (Fig. S1b–f) indicate that the C and O were randomly distributed in the nanoparticles, while the

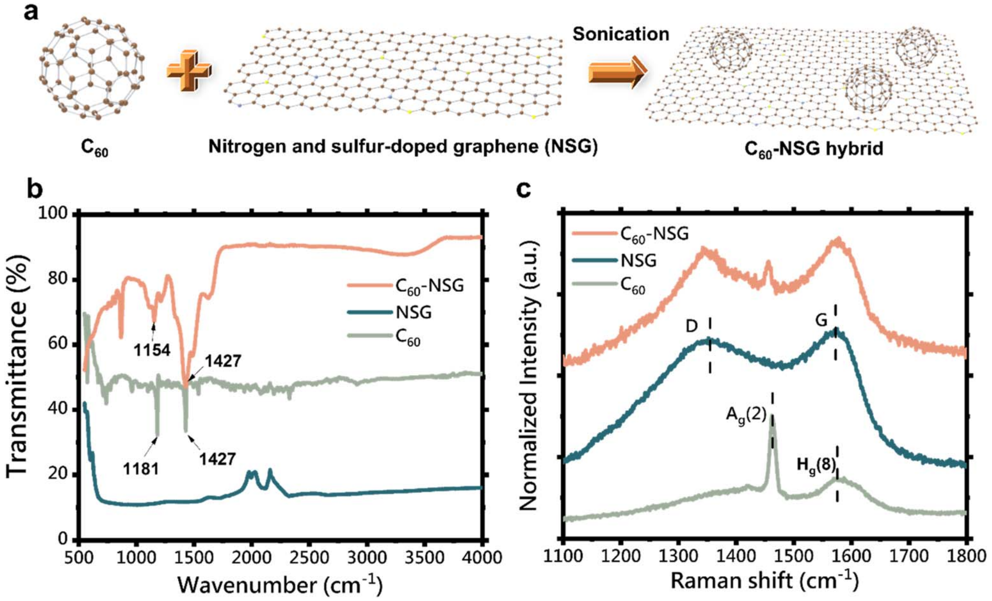

Fig. 1 (a) Schematic diagram of the synthesis of the C_{60}-NSG hybrid. (b) FTIR and (c) Raman spectra of C_{60}-NSG, NSG and C_{60}, respectively.

distribution of N and S was uniform in the C_{60}-NSG. FTIR and Raman spectroscopies further provide evidence for the grafting of C_{60} onto NSG nanosheets. Changes in IR peak positions are observed in the C_{60}-NSG hybrid compared to the individual C_{60} or NSG reference samples (Fig. 1b). The IR peaks at 1427 and 1154 cm^{-1} in the C_{60}-NSG hybrid could be derived from the characteristic IR mode (1427 cm^{-1}) and poly-fullerene clusters (1181 cm^{-1}) of C_{60}, respectively.[59] The relative shift in the IR peak related to the poly-fullerene clusters indicates the functionalization of C_{60} by NSG.[60] The Raman spectrum of the C_{60}-NSG hybrid (Fig. 1c) further reveals three Raman peaks at 1354, 1600 and 1476 cm^{-1}, which correspond to the D (1354 cm^{-1}) and G (1600 cm^{-1}) bands of NSG and the $A_g(2)$ (1476 cm^{-1}) of C_{60}, respectively. The upshift of the G band position in the C_{60}-NSG hybrid compared to pristine NSG indicates charge transfer from the NSG network to the covalently bound C_{60}, resulting from strong electronic interaction between C_{60} and NSG nanosheets.[61] In addition, the chemical bonding properties of C_{60}-NSG were studied from XPS spectra. The high-resolution XPS spectra in Fig. S2 indicate the presence of all the elements, including C, N, and S, for C_{60}-NSG samples. The core level spectrum of C 1s can be deconvoluted into three major peaks, sp^2-hybridized carbon (C–C) (284.6 eV), C–O (287.2 eV), and $\mathrm{O{=}C{-}O}$ (289 eV), as shown in Fig. S2a. The dominant peak of sp^2-hybridized C at 284.6 eV indicates high electronic conductivity and improved charge transfer at the surface.[62] The N 1s core level spectrum in Fig. S2b shows a major peak at 399.9 eV, which corresponds to pyridinic N that creates defects not only at the edge but also on the surface of the graphene nanosheets.[50] One peak at 168.5 eV in the core level S 2p spectrum can be assigned to the $C{-}SO_x{-}C$ species, which are expected to form at the edges of graphene (Fig. S2c).[49]

3.2. Characterization of the C_{60}-NSG hybrid catalytic-protective overlayer on CZTSSe photocathodes

Following successful synthesis of C_{60}-NSG, this hybrid was deposited onto a fresh CZTSSe/CdS sample using the C_{60}-NSG hybrid ink in toluene by spin coating. Due to the ultrathin nature of the C_{60}-NSG hybrid layer, no detectable changes in the morphology of CZTSSe/CdS were observed in SEM analysis (Fig. S3). Similarly, the hybrid layer could not be detected by STEM mapping of CZTSSe/CdS/C_{60}-NSG (Fig. S4) either. All CZTSSe-based photocathodes exhibited comparable absorbance spectra in the visible and near-infrared wavelength regions, regardless of the type of carbon-based hybrid catalytic-protective overlayer used (see Fig. S5). To confirm the successful deposition of these overlayers, XPS analysis was performed on the photocathodes coated with C_{60}, NSG and the C_{60}-NSG hybrid. As shown in Fig. S6, the presence of C 1s, N 1s, S 2p, and Pt 4f signals on the surface of the CZTSSe/CdS/C_{60}-NSG/Pt photocathode confirms the incorporation of the hybrid layer and the Pt catalyst. In addition to XPS, we also used Raman spectroscopy to confirm the deposition of the C_{60}-NSG layer on top of CZTSSe/CdS. As seen from Fig. S7a and b, D and G bands from NSG were determined at around 1354 cm^{-1} and 1600 cm^{-1}. However, the dominant peak at 1476 cm^{-1} from C_{60} was not observed, which might be attributed to the narrow and sharp $A_g(2)$ peak. This assumption is further confirmed by the Raman result of CZTSSe/CdS/C_{60} (Fig. S7c and d), showing the presence of the board peak of $H_g(8)$, but the absence of the sharp peak of $A_g(2)$. The above results manifest that the ultrathin C_{60}-NSG hybrid layer was successfully deposited on CZTSSe/CdS. The hydrophobicity characteristics of CZTSSe/CdS/Pt and CZTSSe/CdS/C_{60}-NSG/Pt were studied by contact angle measurements (Fig. 2a and b), showing that the contact angles increased from 62.68 (CZTSSe/CdS/Pt) to 87.15° (CZTSSe/CdS/C_{60}-NSG/Pt). This means that the surface with the C_{60}-NSG

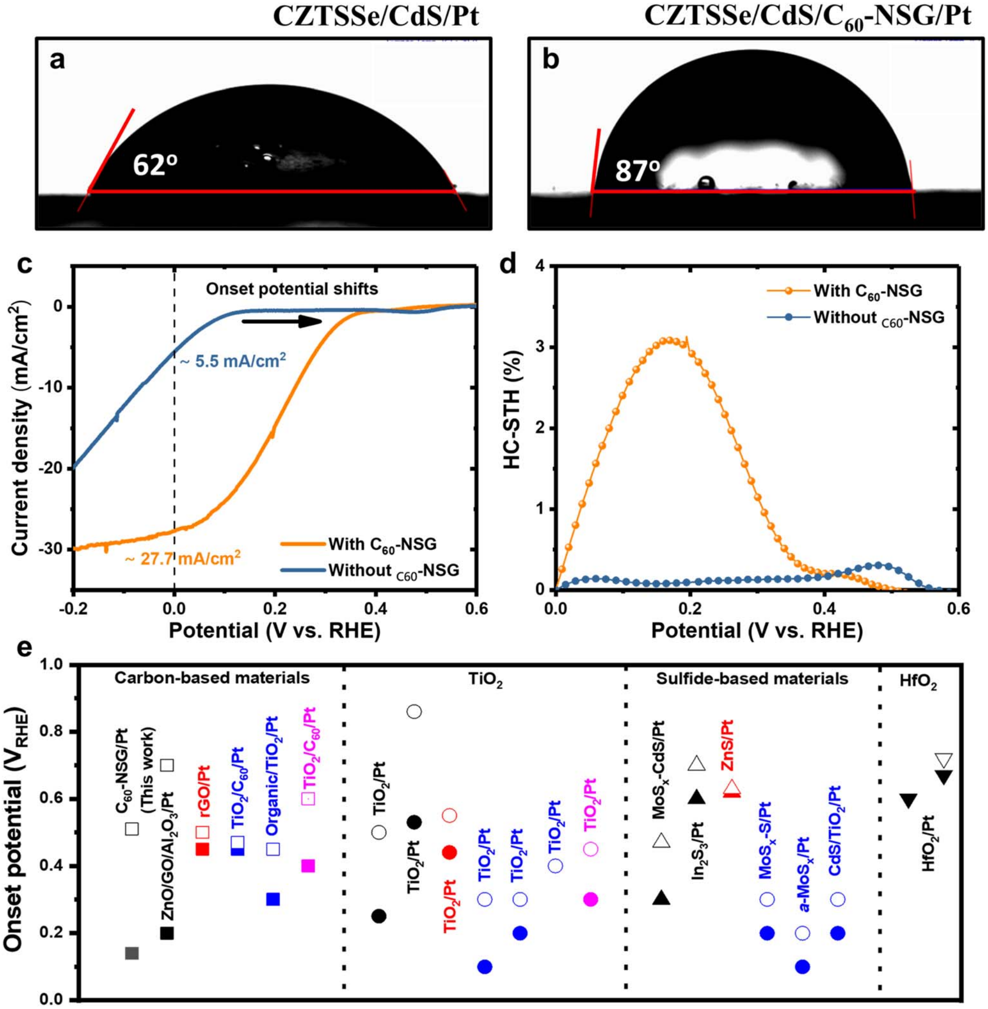

Fig. 2 The contact angle images for (a) CZTSSe/CdS/Pt and (b) CZTSSe/CdS/C_{60}-NSG/Pt. (c) Linear sweep voltammograms of CZTSSe/CdS/C_{60}-NSG/Pt (orange) and CZTSSe/CdS/Pt (blue) photocathodes under light illumination (AM 1.5G) and (d) corresponding HC-STH of the CZTSSe/CdS/C_{60}-NSG/Pt and CZTSSe/CdS/Pt photocathodes. The scan direction is from negative to positive *versus* RHE. (e) A comparison of onset potentials with various overlayers between this work and previously reported kesterite-based water splitting devices. Each symbol shows onset potential with the overlayer (solid symbol) and without the overlayer (hollow symbol).

coating still exhibits hydrophilic characteristics. The surface with hydrophilicity can attract and retain water molecules, creating a microenvironment that enhances the interaction between the electrolyte and the catalyst, thereby improving catalytic efficiency.

The PEC performances of CZTSSe photocathodes with and without the C_{60}-NSG hybrid layer were studied for the HER in a three-electrode configuration in a 0.5 M H_2SO_4 electrolyte (pH = ~0.3) under simulated AM1.5G solar illumination. Fig. 2c shows the current density *versus* potential (*J*–*V*) curves of CZTSSe/CdS photocathodes with and without the C_{60}-NSG hybrid layer under illumination. Both photocathodes were decorated with the Pt catalyst on top. The HER performance of the C_{60}-NSG coated CZTSSe/CdS photocathode (CZTSSe/CdS/C_{60}-NSG/Pt) is much higher than that of the uncoated CZTSSe/CdS photocathode (CZTSSe/CdS/Pt). The CZTSSe/CdS/Pt photocathode has an anodic onset potential (0.14 $V_{\text{reversible hydrogen electrode (RHE)}}$) and achieves a photocurrent density of -5.5 mA cm^{-2} at 0 V_{RHE}. In comparison, the CZTSSe/CdS/C_{60}-NSG/Pt has an anodic onset potential of 0.51 V, that is, ~510 mV relative to $E°(H_2/H_2O)$ and achieves a photocurrent density of -27.7 mA cm^{-2} at 0 V_{RHE}. During the measurement, a large amount of H_2 bubbles evolves on the surface of the photocathodes, as illustrated in Fig. S8. Fig. 2e shows a comparison of onset potential values for both the present and previously reported kesterite-based PEC water splitting devices with various overlayers like carbon-based materials, TiO_2, and sulfide-based materials. The solid and hollow symbols indicate bare photocathodes and overlayers on photocathodes, respectively. The C_{60}-NSG hybrid showed a comparable onset potential value (~0.51 V_{RHE}) to those of previously reported overlayers on kesterite-based photocathodes, indicating efficient charge transfer characteristics.[3] The *J*–*V* curves of both photocathodes with and without the C_{60}-NSG hybrid layer show a negligible current measured under dark conditions (Fig. S9a), implying that parasitic electrochemical reactions are not present in the sample. Furthermore, the calculation of HC-STH using the current density–potential curves reveals that the CZTSSe/CdS/C_{60}-NSG/Pt photocathode demonstrates a HC-STH of ~3% (Fig. 2d). To clarify the individual effects of C_{60} and NSG on PEC performance, CZTSSe photocathodes with the C_{60} or NSG layer were prepared and measured. As shown in Fig. S9b, the NSG layer significantly improves the PEC performance of CZTSSe photocathodes (-20.4 mA cm^{-2}) in comparison with that of the C_{60}-only sample (-8.6 mA cm^{-2}). These results suggest that the overall improvement of PEC performance of the CZTSSe photocathode may mainly arise from the NSG layer rather than the C_{60} layer.

3.3. Mechanism behind enhanced PEC performance

The underlying mechanism of improved PEC performance induced by the C_{60}-NSG hybrid layer is systematically investigated as discussed below. TRPL measurements were performed on CZTSSe photocathodes with and without the C_{60}-NSG hybrid coating. Due to the trapping–detrapping behavior of kesterite, the short component (τ_1) is more related to the real carrier lifetime.[63] Therefore, the τ_1 of photocathodes was fitted by a two-exponential function model (Fig. 3a). The carrier lifetime of the CZTSSe photocathode with C_{60}-NSG is 0.57 ns, higher than that of the reference (0.35 ns), indicating slightly improved electron transfer from the photoexcited kesterite to C_{60}-NSG, which is beneficial for a higher HER activity. Since efficient electron transfer could be attributed to a desirable work function (Φ) between each layer in a photocathode system, ultraviolet photoelectron spectroscopy (UPS) was performed on CZTSSe, CZTSSe/CdS and CZTSSe/CdS/C_{60}-NSG to determine the Φ of CZTSSe, CdS and C_{60}-NSG, respectively. As presented in Fig. 3b, the Φ of CZTSSe, CdS and C_{60}-NSG is 5.38 eV, 5.43 eV and 5.31 eV, respectively. According to the literature, the Φ of sputtered Pt is relatively high, ranging from 5.7 to 6.1 eV, which is significantly larger than that of CdS (5.43 eV).[64] This mismatch can result in the formation of a Schottky-type potential barrier at the CdS/Pt interface, which inhibits efficient electron transfer.[65] In contrast, the C_{60}-NSG hybrid exhibits an intermediate Φ (5.31 eV), positioned between those of CdS and Pt, effectively reducing the potential barrier and facilitating electron transfer. To further validate this, the Φ of C_{60}-NSG was also investigated through DFT calculations of its individual components, estimating theoretical values of Φ of 5.03 eV for C_{60} and 3.74 eV for NSG. These results are consistent with the experimentally measured low Φ value of the C_{60}-NSG hybrid, confirming its role in promoting interfacial charge transfer in the photocathode architecture.

To further understand the catalytic performance of the C_{60}-NSG hybrid and unravel the origin of the catalytic activity of C_{60}-NSG/Pt, DFT calculations were performed. Fig. 3c and S10 depict structural models used to simulate different potential active sites at C_{60}-NSG/Pt interfaces, with N atoms modelled in both graphitic and pyridinic forms, and S atoms modelled in both S–C3 and S–C2 coordination environments. The HER active sites of the C_{60}-NSG/Pt were identified by calculating the free energies of the adsorbed hydrogen at different sites. Fig. 3c depicts the Gibbs free energy change for hydrogen adsorption (ΔG_{H^*}) values for C_{60}-NSG/Pt as well as the pristine C_{60}, and NSG with different N and S atoms. It is well understood that the optimum HER catalyst requires a ΔG_{H^*} value close to zero.[66] The free energy values of adsorbed hydrogen on NSG and C_{60} are far from thermoneutral, resulting in poor H* generation kinetics (ΔG_{H^*} of pyridinic-N = -2.27 eV, S–C2 = -0.82 eV, S–C3 = -2.21 eV and ΔG_{H^*} of C_{60} = 0.50 eV). Graphitic N atoms from the C_{60}-NSG, on the other hand, have a moderate free energy value, bringing them much closer to thermoneutral (-0.17 eV), thus revealing that they could potentially participate as catalytically active sites for the HER process. The Pt site, as expected, performs as a good active site for the HER with free energy very close to thermoneutral (-0.09 eV, hollow site). Thus, overall, the photoexcited electron can be efficiently dispersed from CdS to the Pt catalysts prompted by the conductive C_{60}-NSG hybrid (Fig. 3d) and HER carried out at the active sites discussed above.

3.4. Stability analysis of the CZTSSe photocathode

The stability of CZTSSe/CdS/C_{60}-NSG/Pt photocathodes was monitored by measuring photocurrent density *versus* times under light irradiation at 0.1 V_{RHE} (corresponding to an initial J_{sc} of ~-24.5 mA cm^{-2}) in 0.5 M H_2SO_4 electrolyte. So far, poor stability of the *c*halcogenide photocathodes has been mainly linked to CdS photocorrosion caused by photogenerated holes interacting with the CdS lattice.[67] The PEC of the photocathode could be significantly reduced within a few minutes if there is no embedded protection layer for CdS.[68] The control sample exhibited rapid photocurrent degradation, with a loss of more than 65% within 30 min (see Fig. S11). In contrast, photocathodes with catalytically active layers (CZTSSe/CdS/C_{60}-NSG/Pt) fabricated in this work showed an ~20% photocurrent decay after 10 h of photoelectrolysis under acidic conditions (Fig. 4a). Table S1 shows the PEC performance and stability results of the kesterite photocathodes from the literature. The C_{60}-NSG hybrid overlayer on the CZTSSe photocathode exhibits slower degradation, retaining 96% of PEC performance after around 1 h, compared to 91% for the TiO_2 layer over the same period.[69] To further analyze the photocorrosion behavior of the photocathode, we examined the evolution of the surface composition in the CZTSSe/CdS/C_{60}-NSG/Pt photocathode after a stability test using XPS and STEM characterization. XPS spectra for core-levels for Pt 4f and Cd 3d (Fig. 4b and c) were measured before and after the stability test to determine the amounts of Pt and Cd lost from the CZTSSe photocathode during the HER process. The intensities of Pt 4f and Cd 3d from the CZTSSe photocathode with the C_{60}-NSG layer decreased by about 21% and 13%, respectively after the stability test compared to the original peak intensity. Such loss of Pt catalyst and destruction of the CdS layer are reasons for the gradual reduction of photocurrent density. However, we observe some of the regions without noticeable loss of Pt and CdS layer (Fig. 4d). In other words, the C_{60}-NSG layer might play a role as a Pt catalyst binder as well as a CdS protective layer, provided it achieves better surface coverage of the CdS layer on a rough microstructure of the CZTSSe photocathode. Fig. 4d and e show STEM images and

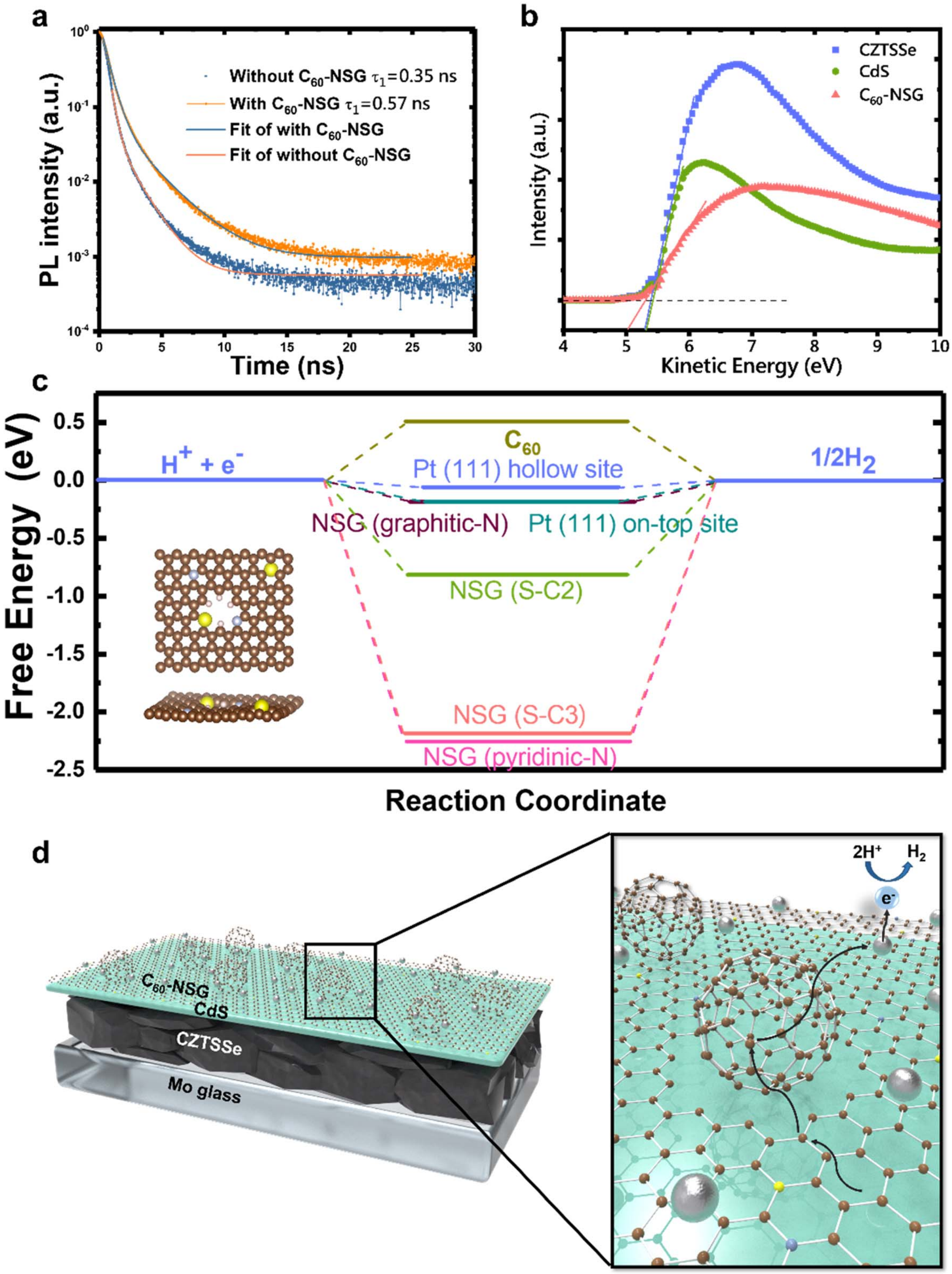

Fig. 3 (a) TRPL at an excitation wavelength of 532 nm for CZTSSe photocathodes with and without the C_{60}-NSG layer. (b) The work function (Φ) of CZTSSe, CdS and C_{60}-NSG measured by UPS. (c) Calculated HER free energy diagrams; inset figures: top and side views of the NSG structural model used in DFT calculations. Brown, blue, yellow, and pinkish-white spheres represent carbon, nitrogen, sulfur, and hydrogen atoms, respectively. (d) The device structure of the CZTSSe/CdS/C_{60}-NSG/Pt photocathode (left) and schematic diagram of the HER at the CZTSSe/CdS/C_{60}-NSG/Pt photocathode (right).

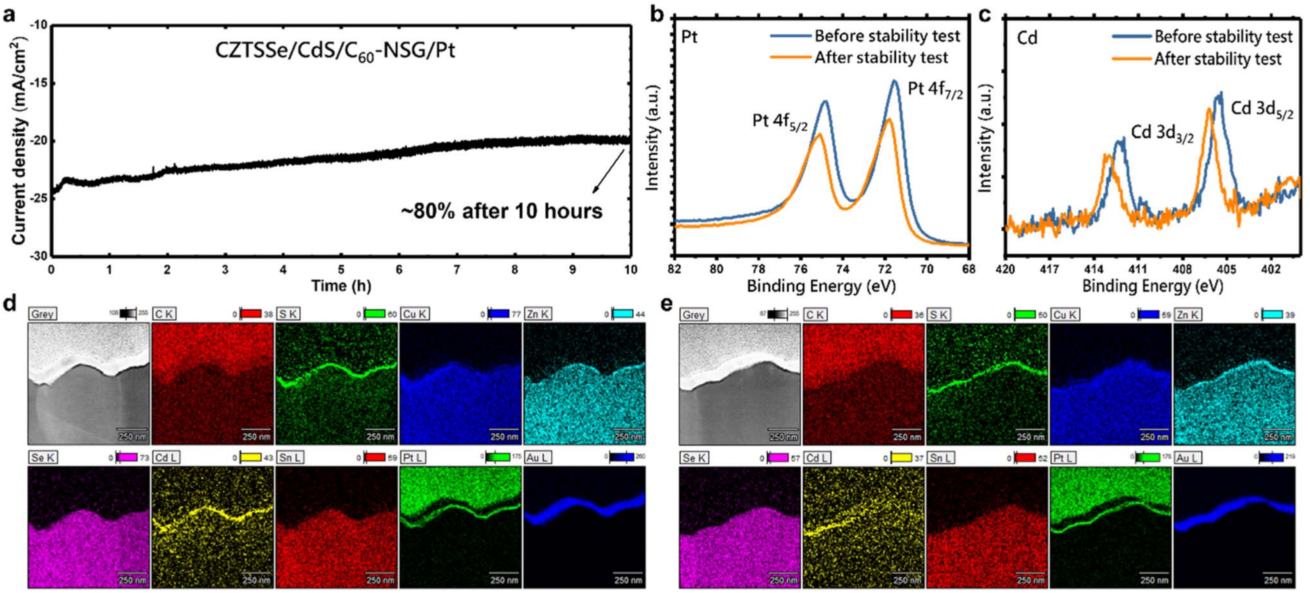

Fig. 4 (a) The stability of the CZTSSe/CdS/C_{60}-NSG/Pt photocathode for 10 h under AM 1.5G illumination at a fixed potential of 0 V_{RHE}. XPS spectra of (b) Pt 4f and (c) Cd 3d taken before and after the 10 h long-term stability test on the CZTSSe/CdS/C_{60}-NSG/Pt photocathodes. (d and e) The two locations of STEM and elemental mapping images of the CZTSSe/CdS/C_{60}-NSG/Pt photocathode after a 10 h stability test.

corresponding elemental mapping images of the photocathode after 10 h stability tests, where we focused on two different interface regions to elucidate the observed photocurrent decay. As shown in Fig. 4d, no noticeable loss of Cd and Pt was observed after 10 h of photoelectrolysis. In contrast, elemental mapping in other regions (Fig. 4e) exhibits no loss of Pt but partial loss of Cd, indicating that the photocorrosion of CdS occurred in the region. The insufficient protection of the CdS layer may be attributed to the limited uniformity and poor surface coverage of the C_{60}-NSG hybrid when deposited *via* spin-coating, particularly on the rough photocathode surface. Nevertheless, the enhanced HER activity and stability of the CZTSSe/CdS/C_{60}-NSG/Pt system can be ascribed not only to the intrinsic catalytic properties of C_{60} and NSG but also to the unique multifunctional characteristics of the C_{60}-NSG hybrid. These include (i) the ability to bind the Pt catalyst, (ii) a pathway for efficient charge collection and transfer to the Pt catalyst; (iii) a protection barrier by reducing photocorrosion of the photocathode in the electrolyte.

Conclusions

In summary, we demonstrate a CZTSSe/CdS/C_{60}-NSG/Pt photocathode that achieves stable and efficient solar water reduction, delivering a high photocurrent density of -27.7 mA cm^{-2} at 0 V_{RHE} and an onset potential of 0.51 V_{RHE}, while retaining 80% its photocurrent after 10 h of sustained photoelectrolysis under strong acid conditions. Comprehensive structural and chemical analyses of the photocathode using Raman, FTIR, TEM, and XPS, conducted before and after stability tests, along with electrochemical studies of the C_{60}-NSG hybrid, revealed its dual role as an effective protective and catalytic overlayer. Spectroscopies characterization combined with DFT calculations confirmed that the improved HER activity and operational stability originate from the unique properties of the C_{60}-NSG hybrid, such as enhanced charge transfer, improved carrier lifetime and effective photocorrosion protection. Furthermore, the C_{60}-NSG hybrid exhibited a near-optimal Gibbs free energy for the adsorbed H species at the identified active sites, facilitating efficient electron transfer to the catalyst surface. The successful integration of the carbon-based 'C_{60}-NSG hybrid' as a protective-catalytic overlayer indicates its broad applicability to various inorganic semiconductor photoelectrodes and offers a promising strategy towards a cost-effective solar-fuel production system.

Conflicts of interest

There are no conflicts to declare.

Data availability

The data supporting this article are available in the SI, which includes additional detailed figures of materials characterization and device performance characterization, as well as supporting tables and notes. See DOI: **https://doi.org/10.1039/d5ta00165j**.

Acknowledgements

M. H., U. S. and S. W. S. contributed equally to this work. M. P. S. acknowledges the Australian Research Council (ARC) for Discovery Early Career Researcher Award (DECRA) (DE210101565). X. H. acknowledges the Australian Research Council (ARC) Future Fellowship (FT190100756). This work was supported by the National Research Foundation of Korea (NRF) grant funded by the Korea government (MSIT) (No. 2022M3J1A1064230). The views expressed herein are those of the authors and are not necessarily those of the Australian Research Council.

References

1 L. Barelli, G. Bidini, F. Gallorini and S. Servili, *Energy*, 2008, **33**, 554–570.
2 A. Haryanto, S. Fernando, N. Murali and S. Adhikari, *Energy Fuels*, 2005, **19**, 2098–2106.
3 M. Suryawanshi, U. V Ghorpade, C. Y. Toe, U. P. Suryawanshi, M. He, D. Zhang, J. S. Jang, S. W. Shin, J. H. Kim and X. Hao, *Prog. Mater. Sci.*, 2023, 101073.
4 T. Hisatomi and K. Domen, *Nat. Catal.*, 2019, **2**, 387–399.
5 D. S. Kim, Y. B. Kim, J. H. Choi, H. W. Suh, H. H. Lee, K. W. Lee, S. H. Jung, J. J. Kim, N. G. Deshpande and H. K. Cho, *Adv. Energy Mater.*, 2021, **11**, 2101905.
6 Y. Ren, F. Nan, L. You, Y. Zhou, Y. Wang, J. Wang, X. Su, M. Shen and L. Fang, *Small*, 2017, **13**, 1603457.
7 R. Mehrotra, D. Oh and J.-W. Jang, *Nat. Commun.*, 2021, **12**, 1–9.
8 J. Kim, S. Seo, J. Lee, H. Choi, S. Kim, G. Piao, Y. R. Kim, B. Park, J. Lee and Y. Jung, *Adv. Funct. Mater.*, 2021, **31**, 2008277.
9 H. Choi, S. Seo, J.-H. Kim, J.-H. Lee, S. Kim, G. Piao, H. Park, K. Lee and S. Lee, *J. Mater. Chem. A*, 2021, **9**, 22291–22300.
10 A. J. Kaufman, R. A. Krivina, M. Shen and S. W. Boettcher, *ACS Energy Lett.*, 2022, **7**, 541–549.
11 D. Zhang, M. Du, P. Wang, H. Wang, W. Shi, Y. Gao, S. Karuturi, K. Catchpole, J. Zhang and F. Fan, *Angew. Chem.*, 2021, **133**, 12073–12079.
12 J. Zheng, Y. Lyu, R. Wang, C. Xie, H. Zhou, S. P. Jiang and S. Wang, *Nat. Commun.*, 2018, **9**, 1–10.
13 H. Kobayashi, N. Sato, M. Orita, Y. Kuang, H. Kaneko, T. Minegishi, T. Yamada and K. Domen, *Energy Environ. Sci.*, 2018, **11**, 3003–3009.
14 M. Chen, Y. Liu, C. Li, A. Li, X. Chang, W. Liu, Y. Sun, T. Wang and J. Gong, *Energy Environ. Sci.*, 2018, **11**, 2025–2034.
15 W. Yang, J. Park, H.-C. Kwon, O. S. Hutter, L. J. Phillips, J. Tan, H. Lee, J. Lee, S. D. Tilley and J. D. Major, *Energy Environ. Sci.*, 2020, **13**, 4362–4370.
16 W. Yang, J. H. Kim, O. S. Hutter, L. J. Phillips, J. Tan, J. Park, H. Lee, J. D. Major, J. S. Lee and J. Moon, *Nat. Commun.*, 2020, **11**, 1–10.
17 S. Grau, S. Giraldo, E. Saucedo, J. R. Morante, A. Llobet and C. Gimbert-Suriñach, *J. Mater. Chem. A*, 2019, **7**, 24320–24327.
18 Y. F. Tay, H. Kaneko, S. Y. Chiam, S. Lie, Q. Zheng, B. Wu, S. S. Hadke, Z. Su, P. S. Bassi and D. Bishop, *Joule*, 2018, **2**, 537–548.
19 S. Y. Reece, J. A. Hamel, K. Sung, T. D. Jarvi, A. J. Esswein, J. J. H. Pijpers and D. G. Nocera, *Science*, 2011, **334**, 645–648.
20 O. Khaselev and J. A. Turner, *Science*, 1998, **280**, 425–427.
21 G. Liang, Z. Li, M. Ishaq, Z. Zheng, Z. Su, H. Ma, X. Zhang, P. Fan and S. Chen, *Adv. Energy Mater.*, 2023, **13**(19), 2300215.
22 C. Yan, J. Huang, K. Sun, S. Johnston, Y. Zhang, H. Sun, A. Pu, M. He, F. Liu, K. Eder, L. Yang, J. M. Cairney, N. J. Ekins-Daukes, Z. Hameiri, J. A. Stride, S. Chen, M. A. Green and X. Hao, *Nat. Energy*, 2018, **3**, 764–772.
23 J. Zhou, X. Xu, H. Wu, J. Wang, L. Lou, K. Yin, Y. Gong, J. Shi, Y. Luo and D. Li, *Nat. Energy*, 2023, 1–10.
24 Y. Gong, Q. Zhu, B. Li, S. Wang, B. Duan, L. Lou, C. Xiang, E. Jedlicka, R. Giridharagopal and Y. Zhou, *Nat. Energy*, 2022, **7**, 966–977.
25 M. Chen, Y. Liu, C. Li, A. Li, X. Chang, W. Liu, Y. Sun, T. Wang and J. Gong, *Energy Environ. Sci.*, 2018, **11**, 2025–2034.
26 L. Li, K. Feng, D. Huang, K. Wang, Y. Li, Z. Guo, Y. H. Ng and F. Jiang, *Chem. Eng. J.*, 2020, **396**, 125264.
27 J. Tan, W. Yang, Y. Oh, H. Lee, J. Park, R. Boppella, J. Kim and J. Moon, *Adv. Energy Mater.*, 2019, **9**, 1–12.
28 K. Wang, Y. Li, L. Li, C. Wang, Y. Fang, W. Zhao, H. Cai, F. Sun and F. Jiang, *Appl. Catal., B*, 2021, **297**, 120437.
29 D. Huang, K. Wang, L. Li, K. Feng, N. An, S. Ikeda, Y. Kuang, Y. Ng and F. Jiang, *Energy Environ. Sci.*, 2021, **14**, 1480–1489.
30 F. Rodríguez-Reinoso and A. Sepúlveda-Escribano, *Carbon Materials for Catalysis*, 2009, pp. 131–155.
31 D. Yu, K. Park, M. Durstock and L. Dai, *J. Phys. Chem. Lett.*, 2011, **2**, 1113–1118.
32 T. He, G. Gao, L. Kou, G. Will and A. Du, *J. Catal.*, 2017, **354**, 231–235.
33 A. R. Puente Santiago, T. He, O. Eraso, M. A. Ahsan, A. N. Nair, V. S. N. Chava, T. Zheng, S. Pilla, O. Fernandez-Delgado, A. Du, S. T. Sreenivasan and L. Echegoyen, *J. Am. Chem. Soc.*, 2020, **142**, 17923–17927.
34 R. Gao, Q. Dai, F. Du, D. Yan and L. Dai, *J. Am. Chem. Soc.*, 2019, **141**, 11658–11666.
35 B. Koo, S. Byun, S. W. Nam, S. Y. Moon, S. Kim, J. Y. Park, B. T. Ahn and B. Shin, *Adv. Funct. Mater.*, 2018, **28**, 1–8.
36 U. Sim, J. Moon, J. Lee, J. An, H. Y. Ahn, D. J. Kim, I. Jo, C. Jeon, S. Han, B. H. Hong and K. T. Nam, *ACS Appl. Mater. Interfaces*, 2017, **9**, 3570–3580.
37 A. Kagkoura, M. Pelaez-Fernandez, R. Arenal and N. Tagmatarchis, *Nanoscale Adv.*, 2019, **1**, 1489–1496.
38 F. Zhang, Y. Chen, W. Zhou, C. Ren, H. Gao and G. Tian, *ACS Appl. Mater. Interfaces*, 2019, **11**, 9093–9101.
39 A. C. Salomao, M. dos Santos Araujo, H. L. S. Dos Santos, M. Medina, L. H. Mascaro and M. A. S. Andrade Junior, *ChemSusChem*, 2021, **14**, 4671–4679.
40 X. Liu, Y. Su, G. Zhang, R. Wang and X. Cai, *Crystals*, 2022, **13**, 66.
41 J. Tan, W. Yang, Y. Oh, H. Lee, J. Park, R. Boppella, J. Kim and J. Moon, *Adv. Energy Mater.*, 2019, **9**, 1900179.
42 B. Koo, S. Byun, S. Nam, S. Moon, S. Kim, J. Y. Park, B. T. Ahn and B. Shin, *Adv. Funct. Mater.*, 2018, **28**, 1705136.
43 M. Legesse, S. N. Rashkeev, F. Al-Dirini and F. H. Alharbi, *Appl. Surf. Sci.*, 2020, **509**, 144893.
44 R. Garg, N. K. Dutta and N. Roy Choudhury, *Nanomaterials*, 2014, **4**, 267–300.

45 G. H. Lee, M. H. Lee, Y. Kim, H.-K. Lim and D. H. Youn, *J. Alloys Compd.*, 2019, **805**, 113–119.

46 K. Gong, F. Du, Z. Xia, M. Durstock and L. Dai, *Science*, 2009, **323**, 760–764.

47 Y. Zhu, L. Gong, D. Zhang, X. Wang, J. Zhang, L. Zhang, L. Dai and Z. Xia, *Nano Energy*, 2019, **63**, 103819.

48 X. Zhu, C. Hu, R. Amal, L. Dai and X. Lu, *Energy Environ. Sci.*, 2020, **13**, 4536–4563.

49 Y. Su, Y. Zhang, X. Zhuang, S. Li, D. Wu, F. Zhang and X. Feng, *Carbon*, 2013, **62**, 296–301.

50 U. P. Suryawanshi, U. V. Ghorpade, D. M. Lee, M. He, S. W. Shin, P. V. Kumar, J. S. Jang, H. R. Jung, M. P. Suryawanshi and J. H. Kim, *Chem. Mater.*, 2021, **33**(1), 234–245.

51 D. Yu, K. Park, M. Durstock and L. Dai, *J. Phys. Chem. Lett.*, 2011, **2**, 1113–1118.

52 G. Kresse and D. Joubert, *Phys. Rev. B:Condens. Matter Mater. Phys.*, 1999, **59**, 1758–1775.

53 G. Kresse and J. Hafner, *Phys. Rev. B:Condens. Matter Mater. Phys.*, 1994, **49**, 14251–14269.

54 G. Kresse and J. Furthmüller, *Phys. Rev. B:Condens. Matter Mater. Phys.*, 1996, **54**, 11169–11186.

55 J. P. Perdew, K. Burke and M. Ernzerhof, *Phys. Rev. Lett.*, 1996, **77**, 3865–3868.

56 A. a. Peterson, F. Abild-Pedersen, F. Studt, J. Rossmeisl and J. K. Nørskov, *Energy Environ. Sci.*, 2010, **3**, 1311.

57 G. Kresse, J. Furthmüller and J. Hafner, *Phys. Rev. B:Condens. Matter Mater. Phys.*, 1994, **50**, 13181.

58 L. Dai and A. W. H. Mau, *Adv. Mater.*, 2001, **13**, 899–913.

59 H. Zhang, L. Fan, Y. Fang and S. Yang, *Chem. Phys. Lett.*, 2005, **413**, 346–350.

60 X. Li, L. Liu, Y. Qin, W. Wu, Z.-X. Guo, L. Dai and D. Zhu, *Chem. Phys. Lett.*, 2003, **377**, 32–36.

61 X. Zhang, Y. Huang, Y. Wang, Y. Ma, Z. Liu and Y. Chen, *Carbon*, 2009, **47**, 334–337.

62 P. Cai, K. Zou, X. Deng, B. Wang, G. Zou, H. Hou and X. Ji, *Front. Chem.*, 2020, **8**, 43.

63 C. J. Hages, A. Redinger, S. Levcenko, H. Hempel, M. J. Koeper, R. Agrawal, D. Greiner, C. A. Kaufmann and T. Unold, *Adv. Energy Mater.*, 2017, **7**, 1700167.

64 E. Bussmann, D. Scrymgeour, M. Brumbach, T. Ohta, S. Smith, H. Hjalmarson, P. Schultz, P. Clem, M. Hopkins and C. Moore, in *APS March Meeting Abstracts*, 2018, vol. 2018, pp. Y31–Y32.

65 E. Watanabe, H. Ushiyama and K. Yamashita, *ACS Appl. Mater. Interfaces*, 2017, **9**, 9559–9566.

66 T. He, G. Gao, L. Kou, G. Will and A. Du, *J. Catal.*, 2017, **354**, 231–235.

67 A. Pareek, A. Gopalakrishnan and P. H. Borse, *J. Phys.: Conf. Ser.*, 2016, **755**, 12006.

68 L. Wei, Z. Guo and X. Jia, *Catal. Lett.*, 2021, **151**, 56–66.

69 C. Ros, *et al.*, *ACS Appl. Mater. Interfaces*, 2018, **10**(16), 13425–13433.